Neural Prediction Model for Transition Onset of a Boundary-Layer in Presence of 2D Surface Defects (ODAS 2022)

Adrien Rouvière, Lucas Pascal, Fabien Méry, Ehouarn Simon, Serge Gratton

ODAS 2022
22th ONERA-DLR Aerospace Symposium
1st to 3rd June 2022 - Hamburg, Germany

Neural Prediction Model for Transition Onset of a Boundary-Layer in Presence of 2D Surface Defects

Adrien Rouviere[(1)], Lucas Pascal[(1)], Fabien Méry[(1)], Ehouarn Simon[(2)] and Serge Gratton[(2)]
[(1)]ONERA / DMPE, Université de Toulouse, F-31055 Toulouse, France, adrien.rouviere@onera.fr
[(2)]Université de Toulouse, INP, IRIT, Toulouse, France

Abstract

Predicting the laminar to turbulent transition is an important aspect of computational fluid dynamics because of its impact on skin friction. Traditional methods of transition prediction do not make it possible to consider configurations where the boundary layer develops in presence of surface defects (bumps, steps, gaps, etc.). A neural network approach is used in this paper, based on an extensive database of boundary layer stability computations in presence of gap-like surface defects. These computations consists on linearized Navier-Stokes calculations and provide informations on the effect of surface irregularity geometry and aerodynamic conditions on the transition to turbulence. Physical and geometrical parameters characterizing the defect and the flow are provided to a neural network whose outputs inform about the effect of a given gap on the transition through the ΔN method.

1 Introduction

In a global context where the general trend is to reduce greenhouse gas emissions, it has become necessary to reduce fuel consumption of future aircrafts. One of the solutions lies in the NLF (Natural Laminar Flow) strategy, which consists on ensuring that pressure gradients on a profile are optimized in order to delay the transition to turbulence. Despite extensive research is carried out about NLF, a laminar boundary layer is hard to obtained due to its high sensitivity to surface imperfections (rivets, junctions, etc.) inherent to the manufacturing processes.

The e^N method [13, 15] is one of the most efficient tool to predict correctly the transition location. The N factor represents the amplification of the boundary layer instabilities and transition occurs when the N factor reaches a critical value N_{tr}. A surface irregularity usually has a localized effect on the vicinity of the defect and is responsible of a N factor shift. Many studies have looked for empirical correlations linking the type of defect and its geometric characteristics to the ΔN shift. Wind tunnel experiments were conducted by Crouch et al. [4] on gaps and by Wang and Gaster [16] on Backward-Facing Steps (BFS). These studies showed that the ΔN corresponded to $0.12b^* \tanh(36\frac{h^*}{b^*})$ for the gaps and $4h^* - 1.40$ for the BFS, where h^* and b^* denote the non-dimensional step height and step width respectively. These empirical relations have the advantage of being simple to implement and not requiring additional experimental or numerical calculations in addition to those required for a smooth surface. On the other hand, each correlation corresponds only to a particular defect geometry and often applies only in a certain range of parameters.

Traditional numerical methods used to predict the transition, such as Local Stability Theory (LST) [11] or Parabolized Stability Equations (PSE) [14], have given satisfactory results for dealing with smooth cases or with surface defects of restricted dimensions. However, the effect of a surface irregularity on the transition is poorly taken into account by these methods because of the assumptions made on the base flow. To overcome these limitations, Worner et al. [17] and Edelmann and Rist [5] used Direct Numerical Simulations (DNS) to study the impact of humps and Forward-Facing Steps (FFS) respectively on the transition. More recently, Franco Sumariva et al. [6] introduced the Adaptive Harmonic Linearized Navier-Stokes (AHLNS) method which they coupled with PSE upstream and downstream of the region with strong streamwise flow variations to study the effect of humps on the transition. A similar technique is used by Hildebrand et al. [9] to study backward-facing steps, by coupling PSE at the inlet domain with Harmonic Linearized Navier-Stokes (HLNS) in the vicinity of the defect.

Nowadays, the rise of Neural Networks (NN) makes it possible to predict instabilities by taking into account many input parameters in a robust manner. Crouch et al. [3] used NN for determining the instability growth rates for calculating the N factors to predict transition caused by crossflow and Tollmien-Schlichting (TS) waves instabilities. Lately, Giannopoulos and Aider [7] predicted the

dynamics of a BFS flow using velocity fields as inputs for a NN. More recently, Zafar et al. [18] proposed a transition model based on convolutional neural networks to predict the growth rates of instabilities in two-dimensional incompressible boundary layers. The same authors also developed a transition model based on recurrent neural networks to predict the N factor envelope as well as the transition position for different wing profiles [19]. The use of artificial NN could allow, due to their architecture, to take into account more complex relations between the geometrical characteristics of a defect in the evaluation of the ΔN compared to the previous empirical correlations.

The aim of this paper is to use NN methods taking into account different geometric and aerodynamic parameters of several types of gap-like surface defects to generate new ΔN models and to make the prediction of the transition to turbulence of a two-dimensional incompressible boundary layer more accurate.

2 Computational strategy

2.1 Governing equations

The flow considered is a boundary layer developing on a flat plate with surface defect and governed by the incompressible two-dimensional Navier-Stokes equations:

$$\boldsymbol{\nabla}\cdot\boldsymbol{u} = 0, \tag{1a}$$

$$\partial_t \boldsymbol{u} + (\boldsymbol{u}\cdot\boldsymbol{\nabla})\,\boldsymbol{u} = -\frac{1}{\rho}\,\boldsymbol{\nabla}\,p + \nu\Delta\boldsymbol{u}, \tag{1b}$$

where $\boldsymbol{u}$ is the velocity vector, p is the pressure, ρ is the fluid density and ν is the kinematic viscosity. The state vector $\boldsymbol{q} = (\boldsymbol{u}, p)$ is decomposed into a steady base flow $\boldsymbol{Q} = (\boldsymbol{U}, P)$ plus an unsteady small perturbations field $\boldsymbol{q'} = (\boldsymbol{u'}, p')$ in the form:

$$\boldsymbol{q}(\boldsymbol{x}, t) = \boldsymbol{Q}(\boldsymbol{x}) + \varepsilon\boldsymbol{q'}(\boldsymbol{x}, t), \qquad \varepsilon \ll 1, \tag{2}$$

where x and y are the streamwise and normal components of the position vector $\boldsymbol{x}$ respectively, and t represents time. Introducing this decomposition into (1), the steady Navier-Stokes equations governing the base flow are obtained:

$$\boldsymbol{\nabla}\cdot\boldsymbol{U} = 0, \tag{3a}$$

$$(\boldsymbol{U}\cdot\boldsymbol{\nabla})\,\boldsymbol{U} = -\frac{1}{\rho}\,\boldsymbol{\nabla}\,P + \nu\Delta\boldsymbol{U}. \tag{3b}$$

At the first order, the LNS equations governing the dynamic of the perturbations developing onto the base flow are written in the form:

$$\boldsymbol{\nabla}\cdot\boldsymbol{u'} = 0, \tag{4a}$$

$$\partial_t \boldsymbol{u'} + (\boldsymbol{U}\cdot\boldsymbol{\nabla})\,\boldsymbol{u'} + (\boldsymbol{u'}\cdot\boldsymbol{\nabla})\,\boldsymbol{U} = -\frac{1}{\rho}\,\boldsymbol{\nabla}\,p' + \nu\Delta\boldsymbol{u'}. \tag{4b}$$

The set of equations (4) is used to calculate the evolution of a small perturbation $\boldsymbol{q'}$ in the boundary layer in a linear regime. Perturbations and forcing term are assumed to be harmonic in time as follow:

$$\boldsymbol{q'}(\boldsymbol{x}, t) = \hat{\boldsymbol{q}}(\boldsymbol{x})\,\mathrm{e}^{-i\omega t}, \tag{5}$$

where $\omega = 2\pi f$ is the real angular frequency of the perturbations and f is the disturbance frequency. Introducing this decomposition into (4), the governing equations of the spatial structure of the perturbations $(\hat{\boldsymbol{u}}, \hat{\boldsymbol{p}})$ are obtained:

$$\boldsymbol{\nabla}\cdot\hat{\boldsymbol{u}} = 0, \tag{6a}$$

$$-i\omega\hat{\boldsymbol{u}} + (\boldsymbol{U}\cdot\boldsymbol{\nabla})\,\hat{\boldsymbol{u}} + (\hat{\boldsymbol{u}}\cdot\boldsymbol{\nabla})\,\boldsymbol{U} = -\frac{1}{\rho}\,\boldsymbol{\nabla}\,\hat{p} + \nu\Delta\hat{\boldsymbol{u}}. \tag{6b}$$

2.2 N factor and ΔN method

Assuming that the TS modes are dependent on both x and y directions, their amplification can be quantified by an infinity norm $A(x)$, *i.e.* the maximum absolute value of the longitudinal velocity along the wall normal coordinate at each position in streamwise direction, as follows:

$$A(x) = \max_y |\hat{u}(x, y)|\,. \tag{7}$$

This method is similar to an e^N method when taking the logarithm of this normalized amplitude:

$$N_f(x) = \ln\left(\frac{A(x)}{A_0}\right), \tag{8}$$

where A_0 is the initial wave amplitude at point x_0 (the critical point at which the instability starts to amplify). Each N_f factor curve is defined for a given non-dimensional reduced frequency F defined as

$$F = \frac{2\pi f\nu}{U_\infty^2} \times 10^6. \tag{9}$$

Since there is no *a priori* knowledge on which frequency will be responsible for triggering transition, an envelope curve of the maximum N_f factors over a large range of frequencies is defined as:

$$N(x) = \max_f N_f(x). \tag{10}$$

The N factor method assumes that the transition occurs at a position x_{tr} for which the envelope curve N reaches a certain threshold value N_{tr}. The ΔN method enables the extension of the e^N method to cases including a surface defect: the N factor for a smooth case configuration is artificially shifted by an additional amplification caused by the defect with a value of ΔN:

$$N = N_{sm} + \Delta N, \tag{11}$$

where N_{sm} is the N factor evaluated for a smooth surface. The transition position is therefore shifted upstream as the threshold value N_{tr} is reached earlier.

2.3 Flow configuration and numerical method

Equations in Section 2.1 are solved by the ONERA's code PIMS2D and the numerical methods used are presented here.

2.3.1 Defect configuration

Different geometries of steps and gaps are studied in this work. The generic parameters defining such defects are two heights h_1 and h_2, the width b and the incompressible boundary layer displacement thickness for a flat plate at zero pressure gradient at the defect location $\delta_{1,d}$. The value of δ_1 at a given position x is given by the semi-analytical Blasius solution $\delta_1(x) = 1.72\sqrt{\frac{\nu x}{U_\infty}}$. This set of 4 parameters is shown in Fig. 1 and aims to geometrically represents any type of gap-like surface defect (cavity, BFS, sequence of BFS and FFS, etc.) in order to standardize the existing correlations linking the geometric parameters to the ΔN. In the rest of this study, the geometrical dimensions of the gap are made non-dimensional by $\delta_{1,d}$ and will be denoted hereinafter h_1^*, h_2^* and b^*, and the aerodynamic parameter defining the position of the defect $\delta_{1,d}$ will be the Reynolds number $Re_{\delta_{1,d}}$.

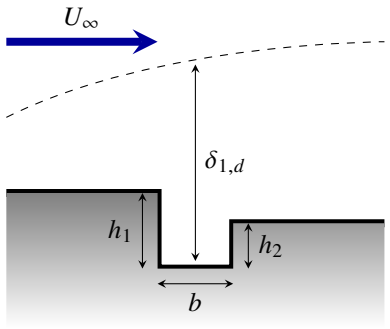

Figure 1: Surface defect parameters.

2.3.2 Base flow

The computational domain extends in the x-direction from an abscissa corresponding to $Re_{\delta_{1,in}} = 350$ to an abscissa corresponding to $Re_{\delta_{1,out}} = Re_{\delta_{1,d}} + 1000$, and in the y-direction over a height $H = 30\delta_{1,out}$. A boundary layer develops and encounters a gap with non-dimensional heights h_1^* and h_2^* and non-dimensional width b^* at an abscissa corresponding to $Re_{\delta_{1,d}}$. No-slip boundary condition is imposed at the wall while a free-slip condition with zero normal-stress is prescribed as an outflow condition. A self-similar boundary layer profile with displacement thickness $\delta_{1,in}$ is imposed at the inlet boundary.

A two-dimensional triangulation of the domain is performed with the FreeFem++ finite element library [8] with a Delaunay–Voronoi algorithm. Equations (3) are discretized with Taylor-Hood finite elements $\mathcal{P}_2$ for the velocity field and $\mathcal{P}_1$ for the pressure. The non-linear solution of the base flow is solved with a classical Newton method, by gradually decreasing the value of the kinematic viscosity from $\nu = 1\,\mathrm{m^2\,s^{-1}}$ until the value corresponding to the desired Reynolds number $Re_{\delta_{1,d}}$ is reached.

2.3.3 LNS computation

Once the base flow is calculated, the TS waves are artificially excited by introducing a volume force term in the LNS equations (4). The computational domain for the LNS calculations is similar to the base flow domain, but has a reduced height of $H = 15\delta_{1,out}$ to avoid having a too large number of vertices. The base flow is thus interpolated on the new mesh and equations (6) are discretized with Taylor-Hood finite elements $\mathcal{P}_2$ for the velocity field and $\mathcal{P}_1$ for the pressure. LNS calculations are performed both on a smooth surface and on a surface with defect, for 91 non-dimensional reduced frequencies in the range $F \in [25, 160]$ to generate the N factor curve. This frequency zone is chosen because it delimits the locally unstable region of a Blasius boundary layer.

2.4 Code validation

To validate PIMS2D in presence of surface imperfection, the configuration studied by Hildebrand et al. [9] is reproduced. The boundary layer meets a BFS of slope $\theta = 75°$ and height $h^* = 0.72$ at the abscissa $x_d = 0.30\,\mathrm{m}$. The flow has the following characteristics: a freestream velocity $U_\infty = 28\,\mathrm{m\,s^{-1}}$, a displacement thickness at the defect location $\delta_{1,d} = 6.90 \times 10^{-4}\,\mathrm{m}$ and a freestream unit Reynold number $Re_\infty = 1.86 \times 10^6\,\mathrm{m^{-1}}$. Figure 2 compares the N factor curves for different frequencies obtained by our method to those obtained by Hildebrand et al. [9]. The results match perfectly with the HLNS calculations and validate PIMS2D in the presence of surface irregularities.

3 Study of a critical step and gap

The study of a critical gap which parameters are detailed in Table 1 is done in this section in order to detail the database generation process for a particular case.

Table 1: Aerodynamic and geometric parameters.

$Re_{\delta_{1,d}}$	h_1^*	h_2^*	b^*
1795.52	1.72	0.47	7.54

Figure 3 shows the pressure distribution at the wall and exhibits a favorable pressure gradient upstream of

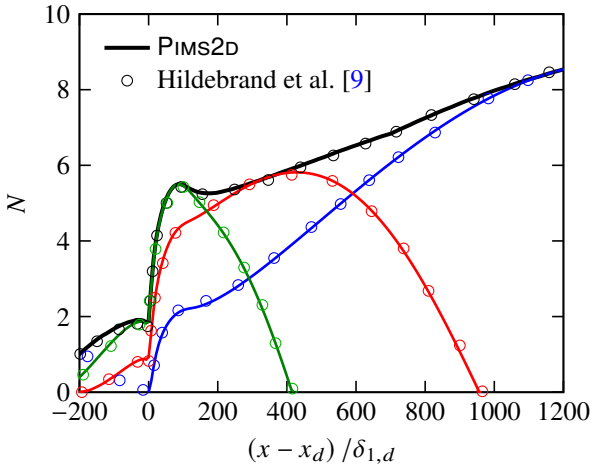

Figure 2: N factor curves for the frequencies $f = 300$ Hz (——), $f = 500$ Hz (——), $f = 700$ Hz (——) and envelope curve (——) for a boundary layer in presence of a BFS.

the gap, followed by a a region with strong adverse pressure gradient and finally a zone with again a favorable pressure gradient approaching towards zero at the infinite downstream of the defect. These pressure variations are responsible for a separation bubble and have an impact on the boundary layer thickness. This one becomes thinner just upstream of the gap when the pressure gradient is negative, and then thickens in the defect. At a certain distance from the gap, the boundary layer recovers the behavior of an unperturbed Blasius boundary layer.

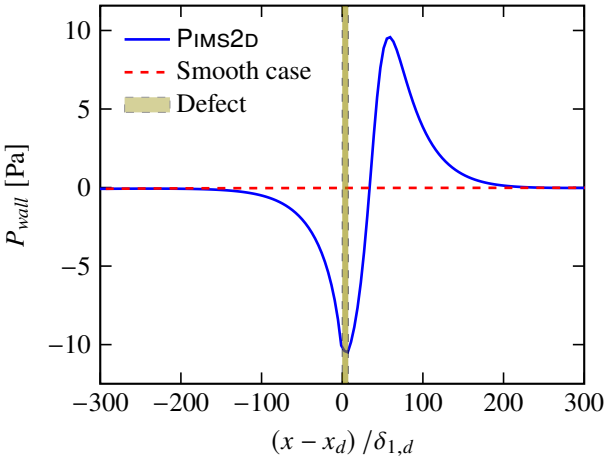

Figure 3: Pressure distribution at the wall within the boundary layer.

Once the base flow is calculated, equations (6) are solved for 91 non-dimensional reduced frequencies in the range $F \in [25, 160]$ and the TS wave amplification curves at the specified frequencies are obtained. The maximum of these amplifications gives the N factor curve shown in Fig. 4. This curve is compared to the N_{sm} curve obtained for a smooth case and allows to visualize quantitatively the effect of a groove on the transition.

At the upstream infinity, the amplification of the perturbations is equivalent with or without irregularity. Slightly upstream of the defect, the favorable pressure gradient region tends to stabilize the disturbances by thinning the boundary layer. However, just after the gap, the N factor increases abruptly to an N_{max} value and recovers the behavior of the flat plate configuration at the downstream infinity but has been shifted by a ΔN_{far} factor.

It is usual to consider that the transition to turbulence occurs when the value of the N factor reaches the threshold value $N_{tr} = 9$ in flight conditions for TS transition scenario. The case considered here is therefore critical in that it triggers turbulence at the defect due to the value of the ΔN_{max}, while the smooth case is always below N_{tr} and therefore remains laminar. The different ΔN values for this case are reported in Table 2.

Table 2: N_{max} and ΔN values for a critical case.

N_{max}	ΔN_{max}	ΔN_{far}
10.10	5.59	3.63

4 Neural network model

4.1 Definition

An artificial neuron is a non-linear function that associates to an input vector $\mathbf{x} = (\mathsf{x}_1, \ldots, \mathsf{x}_n)$ an output y, as follow:

$$\mathsf{y} = \sigma\left(\sum_{i=1}^{n} \mathsf{w}_i \mathsf{x}_i + \mathsf{b}_i\right), \tag{12}$$

where σ is an activation function, $\mathbf{w} = (\mathsf{w}_1, \ldots, \mathsf{w}_n)$ is the vector of connection weights and b is a bias. The activation function introduces non-linearity, allowing the neuron to represent arbitrarily complex functional relations between the input variables and corresponds in this study to a rectified linear unit (ReLU) function defined below:

$$\sigma(z) = \max(0, z). \tag{13}$$

A Neural Network (NN) is a structure composed of successive hidden layers between the input layer and the output layer, where the output of a neuron becomes the input of all the units of the next layer. The learning of the NN consists in iteratively adjusting the weights and biases of the network by minimizing a loss function $\mathcal{L}$.

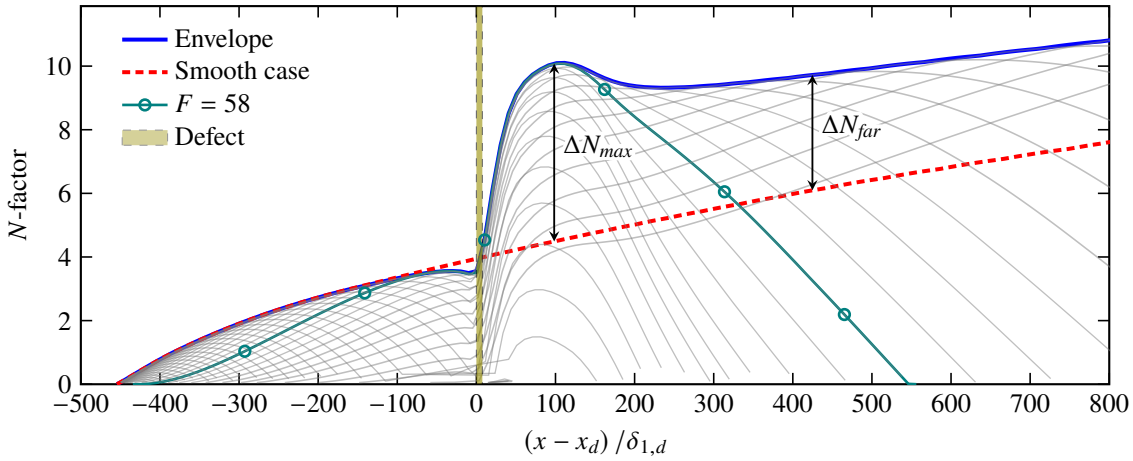

Figure 4: N factor envelope curve with defect (——) and for the same aerodynamic configuration but without defect (- - - -). The figure also shows the amplification curves for all calculated frequencies (——) as well as that of the most amplified frequency (—o—).

4.2 Generation of training data

Inputs of the NN are $Re_{\delta_{1,d}}$ as aerodynamic variable and h_1^*, h_2^* and b^* as geometric parameters. The range of parameters are detailed in Table 3 and have been selected to represent both stable and critical cases that can trigger the transition, according to the criteria defined by Beguet et al. [1]. For each sample of input parameters generated, PIMS2D provides as output the values ΔN_{max} and ΔN_{far}, which will be the outputs to be predicted by the NN.

Table 3: Statistical description of the database with 750 observations.

Parameter	Min	Max
$Re_{\delta_{1,d}}$	901.53	1999.41
h_1^*	0.10	3
h_2^*	0	2.90
b^*	0.52	14.98
ΔN_{max}	0.03	10.71
ΔN_{far}	0.01	6.51

4.3 Database analysis

Figure 5 illustrates the influence of the input geometrical parameters on the ΔN for each case in the database. Analysis of Fig. 5(a) shows that the ΔN_{max} is higher the closer the defect configuration is to a BFS, *i.e.* the higher h_1^* is and the lower h_2^* is. As illustrated in Fig. 5(b), the highest values of ΔN_{max} correspond to the highest b^* when $\Delta h = |h_1^* - h_2^*| < 0.5$. On the other hand, beyond this threshold, the width does not seem to play a determining role and a correlation seems to exist between the heights difference Δh and the value of ΔN_{max}. Moreover, the ΔN_{max} seems to reach a limit around 2 for $\Delta h < 0.5$, *i.e.* for cavities with same heights, while a geometry closer to BFS (high Δh) is more destabilizing. There also appears to be a strong linear relation between the ΔN_{max} and ΔN_{far} values, as shown in Fig. 5(c). This could translate in future studies into the need to know only one of the two ΔN to predict the other.

4.4 Neural network predictions and validation

4.4.1 Implemented neural networks

Neural network with different structures regarding the number of hidden layers and the number of neurons in each layer are considered. The structure of these networks is detailed in Table 4. Each training of the network is done on a normalized training dataset representing 80% of the total dataset (*i.e.* 600 samples) and randomly selected, while the validation is done on the remaining 20% which have never been seen by the network (*i.e.* 150 samples). The loss function to be minimized by the network during the training is defined as the Mean Square Error (MSE) between the real values $\mathrm{y}^{(i)}$ and the values predicted by the neural network $\tilde{\mathrm{y}}^{(i)}$:

$$\mathcal{L} = \frac{1}{n}\sum_{i=1}^{n}\left(\tilde{\mathrm{y}}^{(i)} - \mathrm{y}^{(i)}\right)^2. \tag{14}$$

In order to evaluate the model, the metric used is the Mean Absolute Error (MAE) ϵ_{MAE} described below:

$$\epsilon_{MAE} = \frac{1}{m}\sum_{i=1}^{m}\left|\mathrm{y}^{(i)} - \tilde{\mathrm{y}}^{(i)}\right|, \tag{15}$$

where m is the size of the validation dataset. The results obtained for each network are listed in the Table 4.

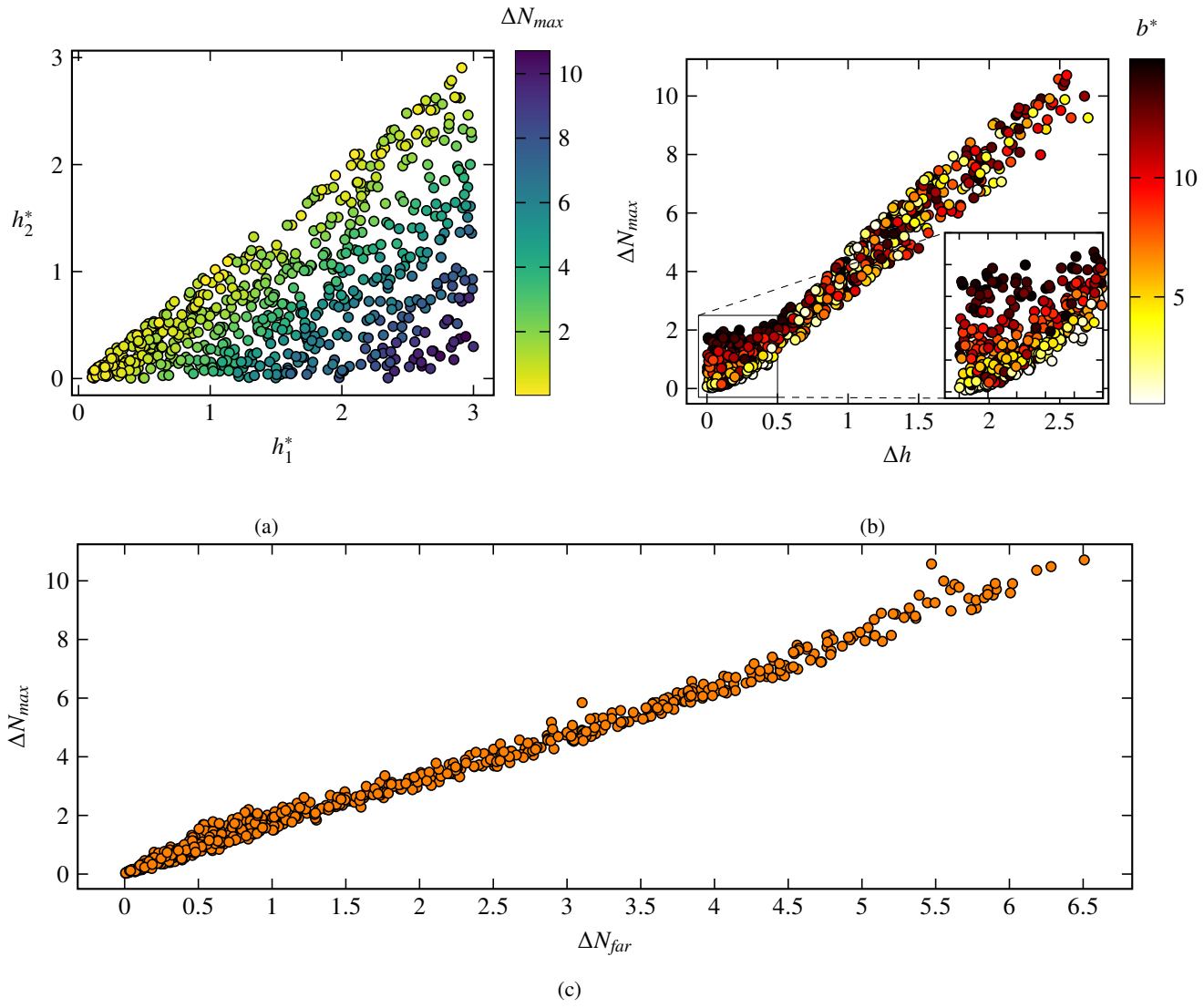

Figure 5: (a)-(b) Evolution of ΔN_{max} as a function of geometric parameters and (c) evolution of ΔN_{far} as a function of ΔN_{max}.

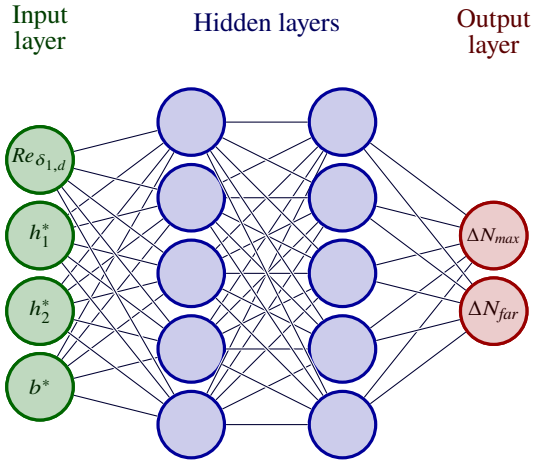

Figure 6: Neural Model methodology.

Table 4: Details of networks architectures and results. Architecture of the network corresponds to the number of neurons in each layer.

Network	Architecture	Parameters	ϵ_{MAE}
$\mathbb{A}$	[4 - 80 - 2]	562	0.07
$\mathbb{B}$	[4 - 20 - 20 - 2]	562	0.09
$\mathbb{C}$	[4 - 15 - 15 - 15 - 2]	587	0.08

4.4.2 Validation of neural network results

Once validated on the validation dataset, the NN model is compared to the experimental results of Crouch et al. [4]. These authors experimentally studied the effect of gaps with identical depths on the transition, for ranges of non-dimensional heights up to 5 and widths up to 50. According [2], the uncertainty on the experimental ΔN value is assumed to be ± 0.15 (± 10 mm on the transition position). An empirical ΔN is proposed from the experiments, which takes into account both the height of the gap and its width. This correlation has the advantage of capturing the limiting behavior between a deep and shallow gap:

$$\Delta N_{Cr} \approx 0.12 b^* \tanh\left(36 \frac{h^*}{b^*}\right). \qquad (16)$$

The comparison between the experimental results, the results from the correlation (16) and the results from the model generated by the neural network $\mathbb{B}$ is shown in Fig. 7. Since the authors of the experimental data did not provide all the data necessary to reproduce their study, the Reynolds number $Re_{\delta_{1,d}}$ is chosen as $Re_{\delta_{1,d}} = 1700$, and the widths chosen are $b^* = 4.3$, 10, 14, 23 and 45 depending on the width range considered. A good agreement is observed between the experimental data and the NN prediction as long as we stay in the range of heights and widths studied by the networks. Outside this range, *i.e.* in the yellow and hatched zones of the graph, corresponding to $h^* \geq 3$ and $b^* \geq 20$, the results are more balanced. For widths studied by the network, the predictions for heights greater than those in the dataset match the experimental results. On the other hand, when the width of the surface irregularity moves away from the range of values known by the network, this one does not predict correctly the ΔN_{max} anymore. However, the experimental points corresponding to $\Delta N_{max} > 6$ probably do not correspond to the transition due to TS waves as explained by the authors, but rather to a bypass transition phenomenon. These points correspond to defect geometries located in the critical zone defined by Beguet et al. [1]. Moreover, as explained by Crouch and Kosorygin [2], a difficulty lies in comparing the values of an experimental ΔN to the values of a numerical ΔN. Indeed, the latter is determined by the global change of the amplification factor in the vicinity of the defect without the knowledge of the actual transition location, while the experimental ΔN is related to the specific modes responsible for the transition. ΔN_{max} results from the NN model seems to reproduce the experimental ΔN whereas one should expect an better agreement with the ΔN_{far}. Unfortunately, only one streamwise position of the gap on the flat plate is available in these experiments. A second position would have give insights on which ΔN to be considered.

Recently, Methel et al. [10] have investigated the effect of gaps and forward facing steps on transition on a flat plate with wall suction at a position corresponding to $Re_{\delta_{1,d}} = 1640$. Some cases without suction have been extracted to be compared to the NN predictions. The agreement between the ΔN_{Exp} obtained experimentally and the ΔN_{far} predicted from the NN is good considering the ϵ_{MAE} value of each neural network. This comparison can be found in Table 5. The last two gaps are out of the training range.

Table 5: Comparison between Methel et al. [10] experimental results without wall suction on a gap and the ΔN_{far} predicted by the neural networks

h^*	b^*	ΔN_{Exp}	$\Delta N_{far\,\mathbb{A}}$	$\Delta N_{far\,\mathbb{B}}$	$\Delta N_{far\,\mathbb{C}}$
1.90	3.80	0.15	−0.06	−0.06	0.17
1.90	12.70	0.34	0.46	0.47	0.58
1.90	22.20	0.96	1.24	1.10	1.50
1.90	28.60	2.20	1.74	1.12	2.28

In order to verify the network's ability to correctly predict the ΔN outside of its training area, Wang and Gaster [16] experimental results on BFS are replicated. The parameter h_2^* is set to zero, while the parameter b^* is set to zero in a first step and set to 20 in a second step, to approximate as closely as possible the geometry of a BFS. A case with $b^* = 0$ is geometrically close to a BFS, while

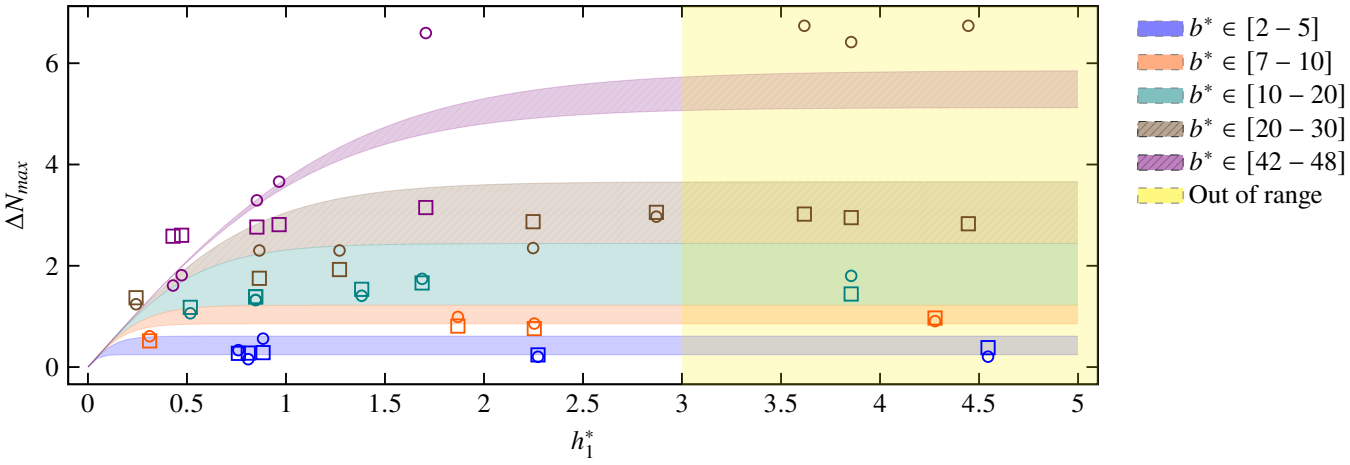

Figure 7: Comparison of the ΔN obtained experimentally by Crouch et al. [4] (○), by the correlation (16) and by the ΔN_{max} predicted by the neural network $\mathbb{B}$ (□). The yellow area (▭) and shaded areas correspond to range of heights and widths that has not been trained by the network.

the $b^* = 20$ case allows us to know if a large distance between a BFS and an FFS amounts to simulating a BFS. Both cases are situated outside the learning area of the networks. The results are plotted in Fig. 8 and show reasonable agreement between the experiment and the neural predictions, keeping in mind that the network has not been trained with a pure BFS configuration. It is interesting to note that the neural results with $b^* = 20$ seem slightly closer to the experimental results when $h_1^* < 1.2$, while beyond this limit the neural results with $b^* = 0$ seem better. In both cases, the observed differences are small and suggest that a "pure" BFS and a succession of BFS and FFS separated by a distance $b^* = 20$ have a similar impact on the boundary layer stability. The NN results corresponding to $Re_{\delta_{1,d}} > 2000$, located outside the training region for the Reynolds number, are represented by filled symbols to differentiate them and have a larger error compared to the experimental results. It is interesting to note that our results are located between the curves corresponding to the Wang and Gaster [16] and Hildebrand et al. [9] correlations on BFS, recalled below:

$$\Delta N_{Wang} = 4h_1^* - 1.4, \tag{17a}$$

$$\Delta N_{Hild} = 3h_1^* - 0.55. \tag{17b}$$

5 Conclusion

A new method for predicting the transition to turbulence of incompressible two-dimensional boundary layers in the presence of gap-like surface defects has been presented. This method is based on the e^N method and a NN is used to determine the value of the ΔN generated by the surface irregularity. The proposed model relies on four distinct parameters defining the geometry of the defect and its aerodynamic environment which are its two heights, its width and the Reynolds number based on the displacement thickness of a Blasius boundary layer at the defect position.

The database was generated with the Pims2d code whose advantage is to be quite flexible in the creation of the studied groove mesh, allowing to easily implement boundary layer stability calculations, while the currently existing methods for the prediction of the transition in presence of defects are rather complex to implement. This code has been validated in the case of a boundary layer around a BFS, showing a good agreement with results from AHLNS calculations.

The average error committed by the model is around 8×10^{-2} on the ΔN , which allows a fairly robust prediction of the criticality of the surface irregularity. Contrary to the empirical correlations already existing in the literature, the model generated by the NN generalizes to any type of gap insofar as the characteristics of the defect are within the range of parameters studied by the network. The parametrization of the surface defects enables to extend the model to other defects, for instance for BFS. Encouraging results have been presented in this sense.

This work can be followed up by a comparison between the results obtained by the NN model and experimental results on step and gap defects carried out in Onera's wind tunnels. The database will be progressively extended to other types of surface defects and will be expanded to take into account the effects of compressibility and pressure gradients.

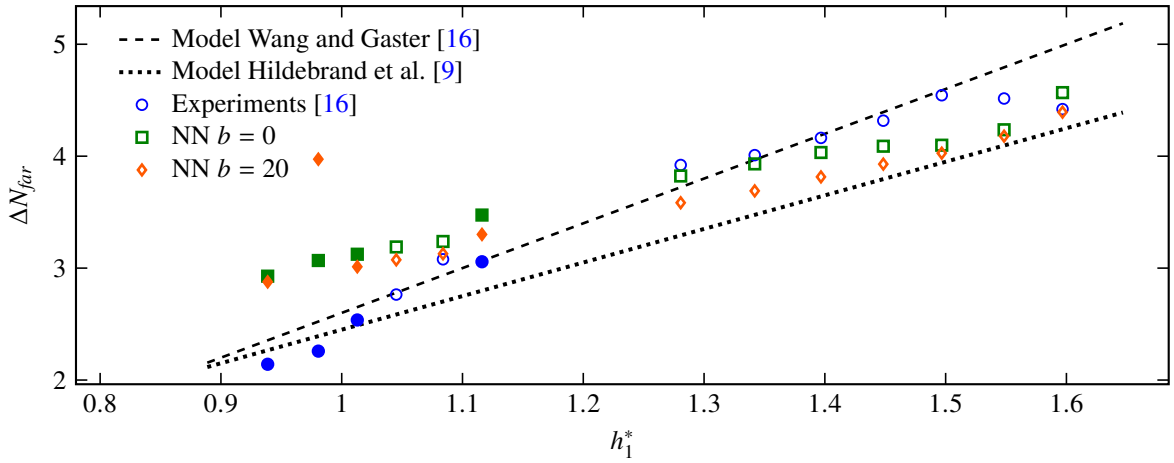

Figure 8: Comparison between predictions of network $\mathbb{B}$, wind tunnel experiments of Wang and Gaster [16] and empirical correlations for BFS. The filled symbols (●■♦) correspond to ranges of $Re_{\delta_{1,d}}$ for which the network has not been trained.

Acknowledgments

This work has been partly funded within the frame of the Joint Technology Initiative JTI Clean Sky 2, AIRFRAME Integrated Technology Demonstrator platform "AIRFRAME ITD" (contract CSJU-CS2-GAM-AIR-2020-945521) being part of the Horizon 2020 research and Innovation framework programme of the European Commission."

Supplementary material

The three networks developed in this paper are available at the following address: https://doi.org/10.5281/zenodo.6074956 [12]. This repository also contains a python script `Main.py` and a jupyter script `Main.ipynb` containing explanations and examples on how to use these NN.

References

[1] S. Beguet, J. Perraud, M. Forte, and J.-Ph. Brazier. Modeling of transverse gaps effects on boundary-layer transition. *Journal of Aircraft*, 54(2):794–801, 2017. doi: 10.2514/1.C033647.

[2] J. D. Crouch and V. S. Kosorygin. Surface step effects on boundary-layer transition dominated by tollmien–schlichting instability. *AIAA Journal*, 58 (7):2943–2950, 2020. doi: 10.2514/1.J058518.

[3] J. D. Crouch, I. W. M. Crouch, and L. L. Ng. Transition prediction for three-dimensional boundary layers in computational fluid dynamics applications. *AIAA Journal*, 40(8):1536–1541, 2002. doi: 10.2514/2.1850.

[4] J.D. Crouch, V.S. Kosorygin, and M. I. Sutanto. Modeling gap effects on transition dominated by tollmien-schlichting instability. In *AIAA Aviation 2020 Forum*, jun 2020. doi: 10.2514/6.2020-3075.

[5] C. A. Edelmann and U. Rist. Impact of Forward-Facing Steps on Laminar-Turbulent Transition in Transonic Flows. *AIAA Journal*, 53(9):2504–2511, September 2015. ISSN 0001-1452. doi: 10.2514/1.J053529.

[6] J.A. Franco Sumariva, S. Hein, and E. Valero. On the influence of two-dimensional hump roughness on laminar–turbulent transition. *Physics of Fluids*, 32(3):034102, 2020. doi: 10.1063/1.5131577.

[7] A. Giannopoulos and J-L. Aider. Prediction of the dynamics of a backward-facing step flow using focused time-delay neural networks and particle image velocimetry data-sets. *International Journal of Heat and Fluid Flow*, 82:108533, April 2020. ISSN 0142-727X. doi: 10.1016/j.ijheatfluidflow.2019.108533.

[8] F. Hecht. New development in freefem++. *J. Numer. Math.*, 20(3-4):251–265, 2012. ISSN 1570-2820. URL `https://freefem.org/`.

[9] N. Hildebrand, M.M. Choudhari, and P. Paredes. Predicting Boundary-Layer Transition over Backward-Facing Steps via Linear Stability Analysis. *AIAA Journal*, 58(9):3728–3734, July 2020. ISSN 0001-1452. doi: 10.2514/1.J059713. Publisher: American Institute of Aeronautics and Astronautics.

[10] J. Methel, M. Forte, O. Vermeersch, and G. Casalis. Experimental investigation on the effect of forward-facing steps and gaps combined with wall suction on boundary layer transition. *Experiments in Fluids*,

63(1):21, December 2021. ISSN 1432-1114. doi: 10.1007/s00348-021-03361-x.

[11] J. Perraud, D. Arnal, and W. Kuehn. Laminar-turbulent transition prediction in the presence of surface imperfections. *International Journal of Engineering Systems Modelling and Simulation*, 6(3-4):162–170, 2014. doi: 10.1504/IJESMS.2014.063129.

[12] A. Rouviere, L. Pascal, F. Méry, E. Simon, and S. Gratton. Neural Prediction Model for Transition Onset of aBoundary-Layer in Presence of 2D Surface Defects, February 2022.

[13] A.M.O Smith and N. Gamberoni. *Transition, Pressure Gradient and Stability Theory*. ARC-19322. Douglas Aircraft Company, El Segundo Division, 1956.

[14] C. Thomas, S.M. Mughal, H. Roland, R. Ashworth, and A. Martinez-Cava. Effect of small surface deformations on the stability of tollmien–schlichting disturbances. *AIAA Journal*, 56(6):2157–2165, 2018. doi: 10.2514/1.J056821.

[15] J.L. van Ingen. A suggested semi-empirical method for the calculation of the boundary layer transition region. *Technische Hogeschool Delft, Vliegtuigbouwkunde, Rapport VTH-74*, 1956. Publieur : Delft University of Technology.

[16] Y. X. Wang and M. Gaster. Effect of surface steps on boundary layer transition. *Experiments in Fluids*, 39 (4):679–686, October 2005. ISSN 1432-1114. doi: 10.1007/s00348-005-1011-7.

[17] A. Worner, U. Rist, and S. Wagner. Humps/Steps Influence on Stability Characteristics of Two-Dimensional Laminar Boundary Layer. *AIAA Journal*, 41(2):192–197, February 2003. ISSN 0001-1452. doi: 10.2514/2.1960.

[18] M.I. Zafar, H. Xiao, M.M. Choudhari, F. Li, C. Chang, P. Paredes, and B. Venkatachari. Convolutional neural network for transition modeling based on linear stability theory. *Phys. Rev. Fluids*, 5:113903, Nov 2020. doi: 10.1103/PhysRevFluids.5.113903.

[19] M.I. Zafar, M.M. Choudhari, P. Paredes, and H. Xiao. Recurrent neural network for end-to-end modeling of laminar-turbulent transition. *Data-Centric Engineering*, 2, 2021. ISSN 2632-6736. doi: 10.1017/dce.2021.11.